JOURNAL OF COMPUTATIONAL PHYSICS 53, 266–288 (1984)

The Ekman Matching Condition in a Partially Filled, Rapidly Rotating Cylinder*

R. J. RIBANDO AND M. A. SHADDAY, JR.†

Department of Mechanical and Aerospace Engineering,
Research Laboratories for the Engineering Sciences,
School of Engineering and Applied Science,
University of Virginia,
Charlottesville, Virginia 22901

Received January 13, 1983; revised July 5, 1983

The use of an analytical matching condition in lieu of grid refinement and direct application of the no-slip boundary condition in a finite-difference calculation is considered for the case of a partially filled, rapidly rotating cylinder. The right circular cylinder is rotating fast enough that the liquid–air interface is nearly vertical. A non-wheel-flow velocity is induced by the differential rotation of the top lid. For the flow conditions of interest, the Ekman boundary layers on the horizontal surfaces are quite thin and their resolution using a very fine mesh makes the overall calculation very time-consuming and costly. We discuss the appropriate form of the Ekman matching condition, which has been widely used in rotating flow theory, to the case of a cylinder which is only partially full, and the fully implicit implementation of that condition into a MAC-derived, time-marching finite-difference calculation. The resulting algorithm is stable and efficient and the results compare quite well with calculations made using grid refinement and direct application of the no-slip condition and with recently published LDV measurements.

INTRODUCTION

In a recent paper Shadday *et al.* [1] reported both experimental and numerical (finite-difference) results for the flow field in a partially filled, rapidly rotating cylinder in which a non-wheel-flow velocity was driven by a differentially rotating top lid. Shadday, using a laser-Doppler velocimeter, measured the axial velocity and the non-wheel-flow part of the azimuthal velocity component. The measured results compared favorably with computed results obtained using a finite-difference simulation of the full, non-linear, axisymmetric governing equations. In Shadday's finite-difference simulation the mesh was refined considerably at the ends in order to give sufficient resolution of the relatively thin Ekman layers.

The presence of $E^{1/3}$ shear layers at both the lateral wall and the free surface as

* Research supported by the U.S. Department of Energy under Contract No. DE-AC05-820R20900.
† Department of Mechanical Engineering, University of South Carolina, Columbia, South Carolina.

0021-9991/84 $3.00

reported in Shadday *et al.* [1] (E being the Ekman number $= \nu/\Omega l^2$) and the investigation thereof can greatly test and extend our understanding of the dynamics of strongly rotating flows. In this paper we examine in particular the application of the Ekman matching condition to flow in a non-full cylinder as an alternative to full resolution of the Ekman boundary layer as was done in Shadday's calculations. We will examine both the theoretical basis and the actual implementation into a finite-difference calculation. In the case of strongly rotating flows, successful implementation of this matching condition can result in at least an order of magnitude saving in computer time, since extremely fine meshes are no longer needed to describe the thin, but crucially important, Ekman layers at either end. Finally, the results obtained using the analytical boundary layer matching in a finite-difference calculation will be shown to compare quite favorably both with results obtained numerically with fully resolved Ekman layers and with experimental measurements.

Problem Formulation

A schematic diagram of the problem which forms the basis of this discussion is shown in Fig. 1. For the experimental runs made, the 19.4-cm-long, 18.9-cm-diam. Plexiglas cylinder was filled to 30% by volume with a glycerin–water solution having a viscosity 10 times that of pure water. The cylinder rotation rate (1000 rpm) was sufficiently high that the free surface was essentially vertical and the upper lid was

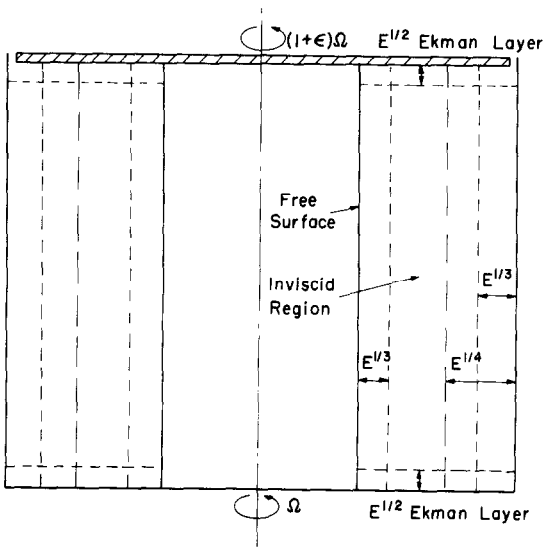

FIG. 1. Schematic diagram of the problem.

oversped by 5%, that is, 50 rpm, to provide the drive for a non-wheel-flow velocity component. More details of the experiment, including the LDV measurement techniques, may be found in Shadday *et al.* [1].

Analysis

An analysis of the problem being considered here has been given by Greenspan [2] and is reproduced in this section. Although not the case in the experiment, we assume for the rest of this section that all boundary layer thicknesses are small relative to the size of the cylinder and the thickness of the fluid layer. Under these asymptotic conditions the flow is divided into an essentially inviscid core and viscous layers at the walls and free surface. With the prescribed conditions, fluid in the horizontal Ekman boundary layer is accelerated radially by centrifugal forces and expelled at the top corner of the cylinder into a sandwich structure of two vertical shear layers. The flow proceeds downward in a sidewall boundary layer to the bottom Ekman layer where fluid is transported radially inward, feeding as it goes, the local, vertical flux required by the top plate. The structures of the Ekman layers depend mainly on the local azimuthal components of interior velocity which here is the basic angular velocity Ω plus half the differential that is imposed at the endplate, the same conditions as when the container is completely filled with liquid. The local Ekman layers, unaware of the air core, transport exactly that amount of fluid that would be appropriate for the filled cylinder. It follows that all the transport that would have ordinarily occurred in the domain which is now an air core, is condensed into a vertical boundary layer at the free interface.

The flow is characterized by the values of three dimensionless parameters: the Rossby number $\varepsilon = \Delta\Omega/\Omega$, the Ekman number $E = \nu/\Omega l^2$ and the radius of the air core a_i (scaled by the height of the cylinder), where ν is the kinematic viscosity of the liquid, Ω is the angular velocity and l is the length of the cylinder.

If a_0 is the dimensionless radius of the cylinder, then it is assumed that E and ε are very much smaller than $1 - a_i/a_0 < 1$ so that a linearized, asymptotic theory is applicable. In this case, the flow is of a boundary layer type and may be described as consisting of the separate domains shows in Fig. 1. The complete, dimensionless governing equations relative to the rotating frame are [3]

$$\frac{1}{r}\frac{\partial}{\partial r} ru + \frac{\partial w}{\partial z} = 0, \tag{1}$$

$$-2v = -\frac{\partial p}{\partial r} + E\left[\frac{\partial}{\partial r}\frac{1}{r}\frac{\partial}{\partial r} ru + \frac{\partial^2 u}{\partial z^2}\right], \tag{2}$$

$$2u = E\left[\frac{\partial}{\partial r}\frac{1}{r}\frac{\partial}{\partial r}(rv) + \frac{\partial^2 v}{\partial z^2}\right], \tag{3}$$

$$0 = -\frac{\partial p}{\partial z} + E\left[\frac{1}{r}\frac{\partial}{\partial r}\left(r\frac{\partial w}{\partial r}\right) + \frac{\partial^2 w}{\partial z^2}\right]. \tag{4}$$

The fluid velocities on the solid walls of the container relative to the rotating frame are

$$\begin{aligned} &u = w = 0,\ v = r \qquad \text{on } z = 1, \\ &u = v = w = 0 \qquad \text{on } z = 0 \text{ and } r = a_0. \end{aligned} \tag{5}$$

Dynamical equilibrium at the interface with the "vacuum" core implies that both pressure and the stress components are zero:

$$\begin{aligned} \frac{\partial}{\partial r}\left(\frac{v}{r}\right) &= 0, \\ \frac{\partial w}{\partial r} &= 0. \end{aligned} \tag{6}$$

Axial symmetry has been invoked and the free surface is assumed to be a circular cylinder, $r = a_i$, so that the kinematic condition at this boundary is

$$u = 0. \tag{7}$$

The inviscid interior flow in the region $a_i < r < a_0$ and valid for ε and E small (when $E^{1/4} \ll 1 - a_1/a_0 < 1$) is given by

$$\mathbf{q}_I = v_I(r)\hat{\theta} + w_I(r)\,\hat{k},$$

where the unknown functions are to be determined.

The Ekman boundary layers at the end caps essentially control the flow since it is through these regions that the forcing is communicated to the body of fluid. The total mass flux in the Ekman layer at any radial position depends on the velocity of the wall relative to that of the interior fluid. It can be shown [3] that the tangential velocities in this boundary layer are given by

$$\begin{aligned} q_r &= -(v_I - V_w)\exp(-\zeta)\sin\zeta, \\ q_\theta &= -(v_I - V_w)\exp(-\zeta)\cos\zeta, \end{aligned} \tag{8}$$

where ζ is a stretched boundary layer coordinate equal to $E^{-1/2}z$ at the bottom and $E^{-1/2}(1-z)$ at the top. The above imply a normal flux from the interior which for the present problem is given by [3]

$$w = -\frac{E^{1/2}}{2r}\frac{\partial}{\partial r}r(v - r) \qquad \text{at } z = 1,\ a_i < r < a_0, \tag{9}$$

$$w = \frac{E^{1/2}}{2r}\frac{\partial}{\partial r}rv \qquad \text{at } z = 0,\ a_i < r < a_0. \tag{10}$$

The total radial mass flux in the boundary layer is obtained from Eq. (8) by integration and is

$$M_T = 2\pi r E^{1/2} \int_0^\infty u \, d\zeta = -\pi r E^{1/2}(v_I - r). \tag{11}$$

The mass flux in the bottom boundary layer is

$$M_B = -\pi r E^{1/2} v_I.$$

Since there can be no radial transport in the inviscid interior $a_i^+ < r < a_0^-$ and the total flux in this direction is zero, it follows that $M_T + M_B = 0$, or

$$v_I = \tfrac{1}{2} r, \qquad w_I = \tfrac{1}{2} E^{1/2}, \tag{12}$$

$$M_T = \tfrac{1}{2}\pi r^2 E^{1/2} = -M_B. \tag{13}$$

Note that the radial flux at r depends only on the local interior value of the azimuthal velocity component. In particular, as $r \to a_i$ which is the free interface, the Ekman layer fluxes are

$$M_T = \tfrac{1}{2}\pi a_i^2 E^{1/2} = -M_B \tag{14}$$

or identical to the values when the cylinder is completely filled and there is no vacuum core. There must then be a vertical flux along the free surface to close the mass transport from the bottom to top Ekman boundary layers whose magnitude is

$$M_{a_i} = \tfrac{1}{2}\pi a_i^2 E^{1/2}. \tag{15}$$

Likewise, at the outer wall $r = a_0$, there must be a net downward flux

$$M_{a_0} = -\tfrac{1}{2}\pi a_0^2 E^{1/2}. \tag{16}$$

These mass transport constraints determine the structure of the vertical boundary layers at these locations.

At $r = a_0$, there are two sidewall boundary layers: an $O(E^{1/3})$ layer required to transport fluid and an $O(E^{1/4})$ layer essential to adjust the azimuthal velocity component to its wall value. At $r = a_i$, however, only an $O(E^{1/3})$ layer develops to meet the flux conditions because the zero stress constraint can be satisfied without the thicker boundary layer. For the conditions of most interest $E^{1/2} \ll E^{1/3} \ll E^{1/4} \ll 1$.

With the preceding analysis the lengthy procedure of calculating the flow in the vertical boundary layer in terms of trigonometric series [3] will yield the rest of the flow field. Rather than evaluate the series, we show in the next section how the preceding analysis may be used in a finite-difference simulation.

Implementation into a Finite-Difference Algorithm

In this section we consider the implementation of the preceding analysis into a finite-difference calculation. In the numerical work reported in Shadday *et al.* [1], the mesh was refined drastically at the horizontal boundaries and the no-slip condition was applied directly. Here instead we apply Eqs. (9) and (10) as equivalent conditions on the interior flow. A similar matching procedure was used at the horizontal surface in Ribando [4] but in that analysis of a flow involving mass injection and removal through the porous sidewall, the Ekman layers were inconsequential anyway. In the present problem the Ekman layers control the flow and are quite thin. Since the allowable timestep for numerical stability is a function of the mesh spacing, there is ample economic incentive for an alternative to mesh refinement in the case of a strongly rotating fluid.

The numerical algorithm used here has been described in detail in Ribando [4] and is essentially a variant of the well-known MAC algorithm [5]. Here we will discuss the overall algorithm briefly and the changes involved in implementing the preceding analysis in detail.

The full axisymmetric, dimensional governing equations written relative to a coordinate system rotating with the container at angular frequency Ω are

$$\frac{\partial u}{\partial t} = -\frac{1}{r}\frac{\partial}{\partial r}(ruu) - \frac{\partial}{\partial z}(uw) + \left(2\Omega + \frac{v}{r}\right)v - \frac{1}{\rho_0}\frac{\partial p}{\partial r} + \nu\left[\frac{\partial}{\partial r}\frac{1}{r}\frac{\partial}{\partial r}(ru) + \frac{\partial^2 u}{\partial z^2}\right], \tag{17}$$

$$\frac{\partial v}{\partial t} = -\frac{1}{r}\frac{\partial}{\partial r}(ruv) - \frac{\partial}{\partial z}(vw) - \left(2\Omega + \frac{v}{r}\right)u + \nu\left[\frac{\partial}{\partial r}\frac{1}{r}\frac{\partial}{\partial r}(rv) + \frac{\partial^2 v}{\partial z^2}\right], \tag{18}$$

$$\frac{\partial w}{\partial t} = -\frac{1}{r}\frac{\partial}{\partial r}(ruw) - \frac{\partial}{\partial z}(ww) - \frac{1}{\rho_0}\frac{\partial p}{\partial z} + \nu\left[\frac{1}{r}\frac{\partial}{\partial r}\left(r\frac{\partial w}{\partial r}\right) + \frac{\partial^2 w}{\partial z^2}\right], \tag{19}$$

$$\frac{1}{r}\frac{\partial}{\partial r}(ru) + \frac{\partial w}{\partial z} = 0. \tag{20}$$

The pressure has been combined with the centrifugal acceleration to form the reduced pressure appearing above [3].

The mesh system employed in the finite-difference solution of the above equations is shown in Fig. 2. Pressure is defined at the center of the primary control volumes; control volumes for the radial and vertical velocity are shifted a half grid space to the right and a half grid space upward, respectively. To facilitate a substitution used later, the azimuthal velocity has been defined at the same point as the radial velocity.

In an abbreviated form Eqs. (17), (18), and (19) are differenced as

$$\frac{u_{i,j}^{N+1} - u_{i,j}^{N}}{\Delta t} = \text{Convection}^{N}_{i,j} + 2\Omega v_{i,j}^{N+1} + \text{Curvature}^{N}_{i,j} + \frac{1}{\rho_0}\frac{p_{i,j}^{N+1} - p_{i+1,j}^{N+1}}{\Delta r} + \text{Viscous}^{N}_{i,j}, \tag{21}$$

$$\frac{v_{i,j}^{N+1} - v_{i,j}^{N}}{\Delta t} = \text{Convection}^{N}_{i,j} - 2\Omega u_{i,j}^{N+1} + \text{Curvature}^{N}_{i,j} + \text{Viscous}^{N}_{i,j}, \tag{22}$$

$$\frac{w_{i,j}^{N+1} - w_{i,j}^{N}}{\Delta t} = \text{Convection}^{N}_{i,j} + \frac{1}{\rho_0}\frac{p_{i,j}^{N+1} - p_{i,j+1}^{N+1}}{\Delta z} + \text{Viscous}^{N}_{i,j}, \tag{23}$$

where the superscripts N and $N+1$ indicate the present and advanced time levels, respectively.

With the radial and azimuthal velocities defined at the same point, Eq. (22) may be used to eliminate $v_{i,j}^{N+1}$ in Eq. (21). This leaves one equation involving only the variables $u_{i,j}$ and $p_{i,j}$ at the advanced level. Requiring continuity to be satisfied at the new time level (and ignoring curvature only for purposes of this discussion), Eq. (20) in difference form becomes

$$u_{i-1,j}^{N+1}\,\Delta z - u_{i,j}^{N+1}\,\Delta z + w_{i,j-1}^{N+1}\,\Delta r - w_{i,j}^{N+1}\,\Delta r = 0. \tag{24}$$

Equation (21) with $v_{i,j}^{N+1}$ eliminated using the substitution discussed, an analogous expression for $u_{i-1,j}^{N+1}$, Eq. (23) for $w_{i,j}^{N+1}$ and an analogous expression for $w_{i,j-1}^{N+1}$ are substituted into Eq. (24) to obtain a Poisson equation for pressure at the new time level.

The complete computational sequence is

1. Update explicit terms (convection, viscous, curvature) in Eqs. (21), (22), and (23).

2. Substitute Eq. (22) into (21) and solve for $u_{i,j}^{N+1}$.

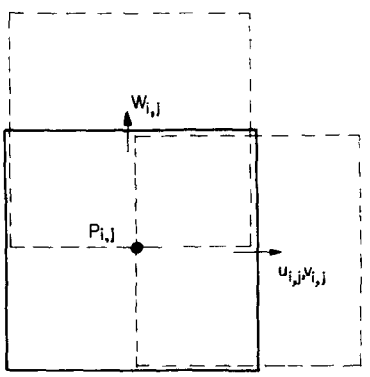

FIG. 2. Nodal volumes used in the finite-difference calculation for pressure and the three velocity components.

3. Substitute Eq. (23) and the modified Eq. (21) and their counterparts at $w_{i,j-1}$ and $u_{i-1,j}$ into Eq. (24).

4. Solve resulting Poisson equation for pressure.

5. Update all velocities using new pressure field.

6. Update all explicit boundary conditions.

7. Increment time and repeat until steady state is reached.

Since this calculation does represent a true transient, the total number of timesteps needed is simply the length of the transient (typically a small multiple of the spinup time scale, an estimate of which is given in Greenspan [3]) divided by the timestep used. As an example, for the calculation corresponding to Shadday's experimental work, approximately 500 timesteps were used.

A direct method (Gauss elimination [6]), has been used to solve the Poisson equation in step 4; thus there is no iteration at all in this scheme. Also in substituting the momentum equations into the continuity equation, the divergence at the previous time level has been retained at all internal cells [5]. The treatment at the ends discussed later is predicated on the net flow out at either end being identically zero at each timestep. Thus no divergence control problems have arisen.

As in Ribando [4] the Coriolis terms have been treated fully implicitly rather than explicitly as in Beardsley *et al.* [7] and others. The present implicit treatment of all the terms in that subset of the full governing equations which describes inviscid inertial waves [3] is analogous to the treatment of acoustic waves in the ICE (implicit continuous-fluid Eulerian) technique described by Harlow and Amsden [8] and Hirt and Nichols [9]. Analogous benefits in terms of allowable timestep and absence of truncation error-induced waves may be expected.

The treatment of the inner free shear boundary is unchanged from Ribando [4]. Shear due to the air in the "vacuum" core has been neglected as have surface tension effects. The inner free boundary has been allowed to move radially a small fraction of a grid space; under the conditions of interest here, the displacement is miniscule. The fully implicit treatment of this displacement is described fully in [4]. The application of the no-slip condition at the outer vertical sidewall is straightforward. At the horizontal boundaries the appropriate conditions are Eqs. (9) and (10) written here in dimensional form [3]:

$$w_T = -\frac{1}{2}\left(\frac{\nu}{\Omega}\right)^{1/2}\frac{1}{r}\frac{\partial}{\partial r}r(v_T - V_T) \qquad \text{at } z = z_T, \tag{9'}$$

$$w_B = \frac{1}{2}\left(\frac{\nu}{\Omega}\right)^{1/2}\frac{1}{r}\frac{\partial}{\partial r}rv_B \qquad \text{at } z = z_B. \tag{10'}$$

Here as before, V_T is the relative (overspeed) velocity between the top disk and the rotor. In Ribando [4] the Ekman flows were treated explicitly; that is, $w^{N+1} = f(v^N)$. The separable pressure Poisson was solved using cyclic reduction. In the present case the Ekman layers drive the flow and a fully implicit of the Ekman flow would appear

to be more appropriate. The advanced time level azimuthal velocities appearing on the right-hand sides of Eqs. (9′) and (10′) may be expressed using Eq. (22) in terms of the advanced time level radial velocities at the same location (Fig. 2). Note that the Ekman suction flow is thus dependent on the pressure gradient along the boundary rather than on an axial gradient, the normal situation for an axial velocity component. The finite-difference expressions arising from Eqs. (9′) and (10′) replace the forms for $w_{i,j}^{N+1}$ and $w_{i,j-1}^{N+1}$ which normally come from Eq. (23), at the top and bottom, respectively, in Step 3 of the calculational procedure. The result is that the coefficients of the horizontal terms in the pressure equation are slightly different at the top and bottom rows of cells from what they are in the rest of the field. The linear equations resulting from this non-separable Poisson-like equation may be readily solved using Gauss elimination. Unless the timestep is being changed during the calculation, the decomposition of this large, banded system needs to be done only once, at the first timestep.

Let us consider in more detail the finite-differencing of Eqs. (9′) and (10′) in view of Fig. 2. We will consider the solid rectangle in Fig. 2 as one of the cells comprising the first row along the bottom of the cylinder. The (axial) flow through the lower face is the Ekman suction flow given by Eq. (10′). Because of the staggered mesh the interior values of the azimuthal velocity, which appear in Eq. (10′), are defined a half grid space above the lower edge. These interior values of azimuthal velocity are computed in the normal way. As in the interior of the flow the new azimuthal velocity is expressed in terms of the new radial velocity using Eq. (22). In both the radial and azimuthal momentum equations the shear stress acting on the lower faces which involve axial derivatives are negated by applying a "slip" condition; the effect of the "no-slip" boundary having already been taken into account by use of the compatibility relation (Eq. (10′)). Axial shear stress terms are operative in the interior of the fluid.

The finite-difference representation of Eq. (10′) is

$$(2\pi)\, w_{B_i} r_{m_i} \Delta r_i = \frac{1}{2}\left(\frac{\nu}{\Omega}\right)^{1/2} (r_i v_{B_i} - r_{i-1} v_{B_{i-1}})\, 2\pi,$$

where both sides have been multiplied by 2π. The summation of the left side across the radius is the net flux out the Ekman layer and ought to equal zero. In summing the right-hand side we note that internal to the flow there will be pair-by-pair cancellation; that is, the term coming from the right-hand side of a cell will cancel with the term coming from the left-hand side of the cell to its right. Under certain conditions there may, however, be terms left over at the ends. These "leftovers" are precisely the sources and sinks discussed earlier in the analysis section.

At the free surface, for instance, at the bottom the leftover term is $-\pi(\nu/\Omega)^{1/2} r_{i-1} v_{B_{i-1}}$; at the top the leftover term is $-\pi(\nu/\Omega)^{1/2} r_{i-1}(v_{T_{i-1}} - V_{T_{i-1}})$ which is equivalent to Eq. (11). At the outer wall there is no leftover term at the bottom. At the top there is a term due to the slip between the differentially rotating lid and the rotor; i.e., $\pi(\nu/\Omega)^{1/2} r_i V_T$, which provides another source.

The general guideline is to finite-difference Eqs. (9′) and (10′) so that terms cancel pair-by-pair in the middle, but at the ends force mass conservation into and out of the Ekman layer by dropping the leftover terms wherever they appear. This automatically will create the sources and sinks as appropriate. For a full rotor we note that there would be no leftover terms at the center; there would be at the outer edge of a differentially rotating lid. For a spinup problem involving a full rotor and no-slip walls, there would be no sources or sinks at all.

Results

The procedure just described was incorporated into the same computer program used in Ribando [4] and Shadday *et al.* [1]. The same parameters as were used by Shadday in his experiment and in his finite-difference solution using fully resolved Ekman layers were employed. These include the container speed (1000 rpm), the top lid speed (1050 rpm), the rotor length (10.4 cm), the inside diameter (18.0 cm), the conditions $E = 2.5 \times 10^{-}$. The radial grid spacing used was identical to Shadday's. The 20 radial spacings ranged from 0.07 cm at the edges to 0.15 cm at the center of the fluid layer. The radial resolution was sufficient to give approximately four grid-points in the characteristic distance $E^{1/3}L$ inward from the wall and free surface, a distance equal to about 15% of the film thickness. Shadday's 31 axial spacings ranged from 0.02 cm at the ends to 1.6 cm at the middle; here the 31 axial spacings were a uniform 0.627 cm. The spinup time scale $((L^2/\Omega\nu)^{1/2})$ [3] for this case is about 6 sec; this calculation was run out to 12.1 sec. In this and all other cases run the 5% overspeed was ramped in over a period of 1 sec.

Figure 3a shows the streamlines resulting from Shadday's calculations using fully resolved Ekman layers; Fig. 3b shows streamlines resulting from the present calculation using matching. Both streamfields were obtained by integrating the vertical velocity; the increment is a uniform 0.61×10^{-6} m^2/sec. The left edge in these and all succeeding contour plots is the free surface, not the centerline. In these two plots the horizontal coordinate has been expanded by a factor of 7.3 to better depict the structure of the vertical boundary layers. Contours of constant azimuthal velocity for the two calculations are presented in Figs. 4a and b; the increment is 0.037 m/sec. The "matched" results in Figs. 3b and 4b of course lack the details within the Ekman layers seen in the fully resolved results, but the agreement outside the Ekman layers is quite good in both sets of plots. In Figs. 5 and 6 we compare Shadday's experimental measurements, his calculated values using resolved Ekman layers, and the present calculations using Ekman layer matching at two of the four axial locations where he took measurements. In all cases the results are non-dimensionalized by the peripheral speed of the top lid. The two calculations are seen to give comparable results, which compare well with experimental values. Discrepancies at the free surface between the LDV measurements and finite-difference solution have been discussed at length in Shadday *et al.* [1].

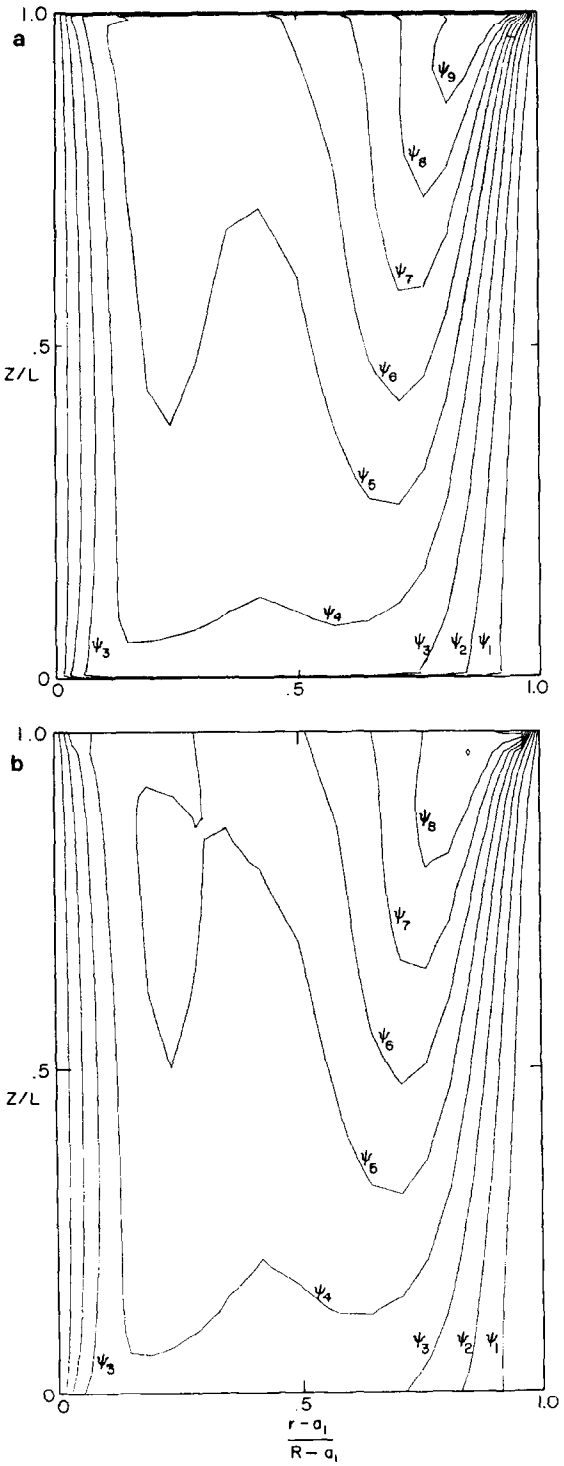

FIG. 3. Streamlines calculated using resolved Ekman layers (a) reproduced from Shadday *et al.* [1] and matched Ekman layers (b). $E = 2.5 \times 10^{-6}$. Horizontal scale expanded by a factor of 7.3. Streamline increment $= 0.61 \times 10^{-6}$ m^2/sec. In this and succeeding plots the left edge is the free surface, not the centerline.

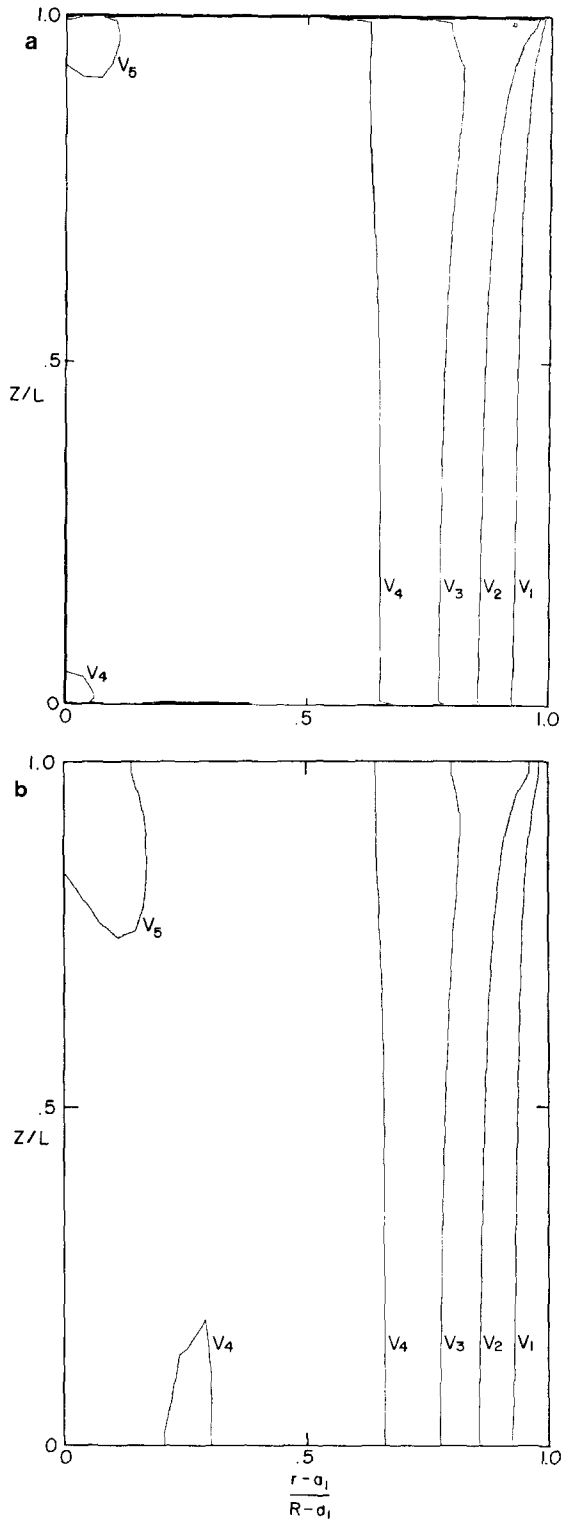

FIG. 4. Contours of constant azimuthal velocity using resolved Ekman layers (a) reproduced from Shadday *et al.* [1] and present calculation using matching (b). Parameters same as in Fig. 3. Contour increment = 0.037 m/sec.

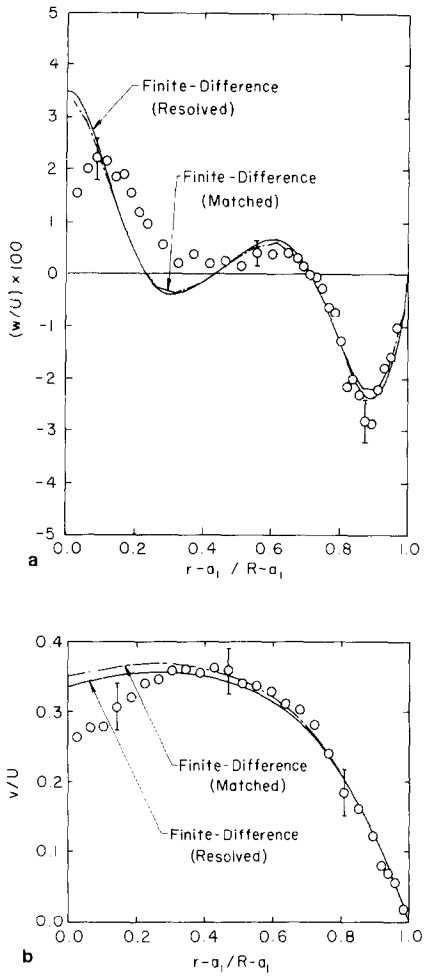

FIG. 5. Radial profiles of the axial and azimuthal velocities at $z/L = 0.438$ corresponding to the flows of Figs. 3 and 4 and Shadday's experimental results.

Since the flow is nearly linear, the timestep in both cases is limited by the explicit treatment of the diffusion terms ($\Delta t \leqslant \min_{i,j}(1/2\nu(1/\Delta r^2 + 1/\Delta z^2))$). The larger minimum grid spacing in the present case resulted in a dramatic savings in computer time. The maximum allowable timestep was increased by a factor of about 13 in this case; with the computer time per timestep roughly equal, the total computer time decreased by about the same factor. The total computer time for the case using matching was 505 sec on a CDC Cyber 730.

Shadday's measurements and the calculations presented thus far involve a relatively thin layer; that is, there is no inviscid region separating the shear layers. In Figs. 7 and 8 we present results for layers double and triple the thickness used by

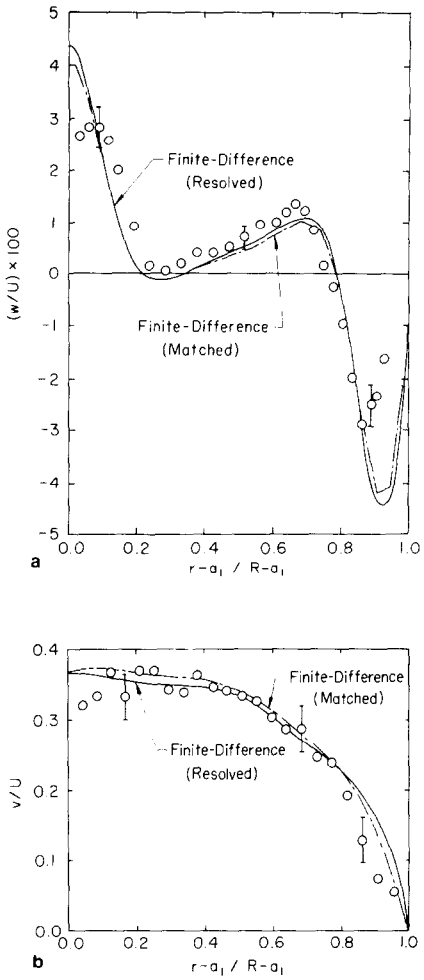

FIG. 6. Radial profiles of the axial and azimuthal velocities at $z/L = 0.830$ corresponding to the flows of Figs. 3 and 4 and Shadday's experimental results.

Shadday. All parameters, including the Ekman number, are as before; only the fill ratio and thus a_i are changed. The vertical mesh used was the same as before. Rather than use more horizontal mesh points, the grid was expanded in the center, with, of course, a slight degradation in accuracy. Again, about four gridpoints were retained in the distance $E^{1/3}L$ in from the sides, a characteristic length which stays constant for these three runs, but which becomes a smaller fraction of the film thickness as the latter increases. Seven or eight gridpoints were spaced over the entire shear layer thickness. In the plots the horizontal scales have been expanded by factors of 3.6 and 2.4, respectively, to produce a uniformly sized plot. The streamline plots (Fig. 7a and

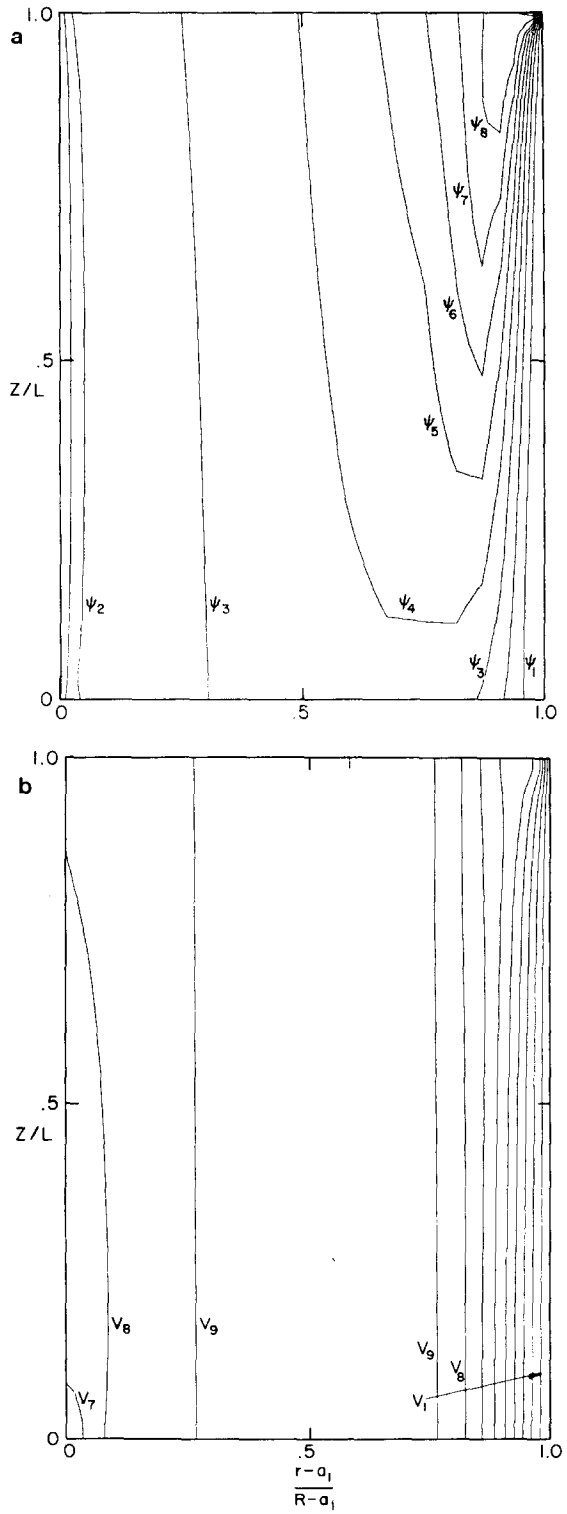

FIG. 7. Streamlines and azimuthal velocity contours for same conditions as Fig. 3b, but film thickness doubled. Horizontal scale expanded by a factor of 3.6. Streamline increment = 0.61×10^{-6} m^2/sec. Azimuthal velocity contour increment = 0.0189 m/sec.

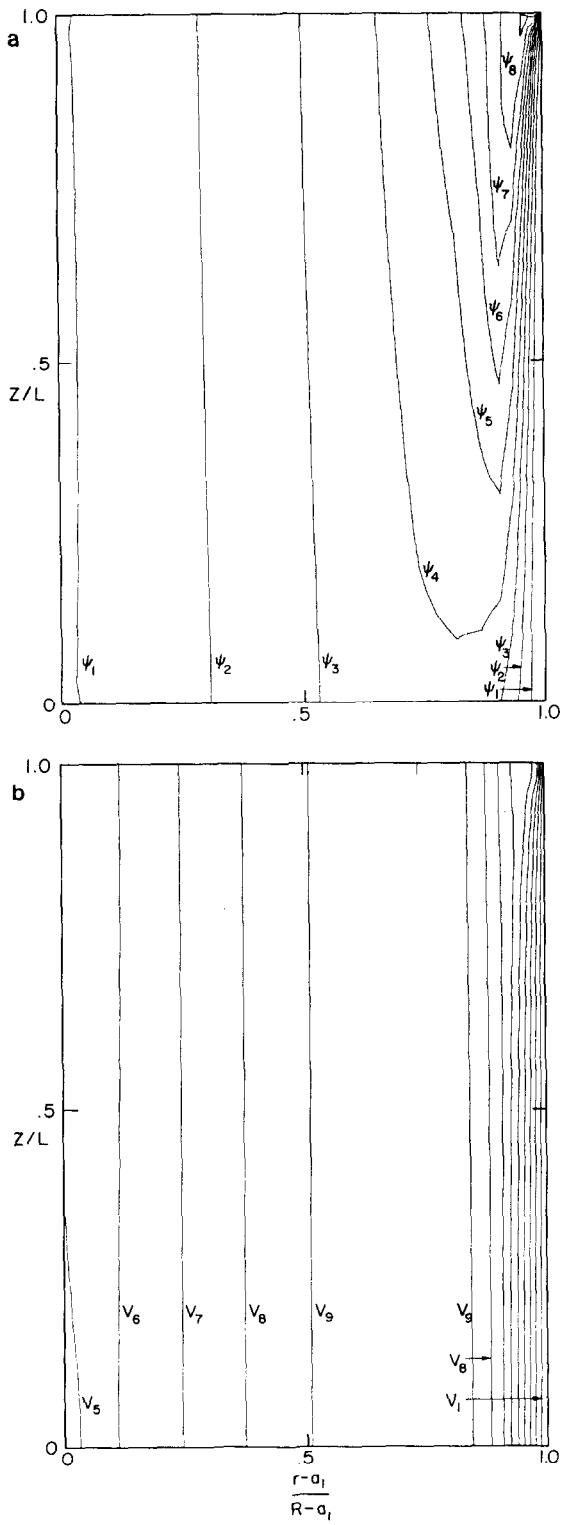

FIG. 8. Streamlines and azimuthal velocity contours for same conditions as Fig. 3b, but film thickness tripled. Horizontal scale expanded by a factor of 2.4. Streamline increment $= 0.60 \times 10^{-6}$ m^2/sec. Azimuthal velocity contour increment $= 0.0189$ m/sec.

in particular Fig. 8a) show clearly an interior region of uniform upflow. These same results are shown more dramatically in Fig. 9, where the axial velocity at midheight has been plotted as a function of radius for the three film thicknesses studied. The wall shear layer is virtually the same in all cases. Again a uniform region of upwelling is evident in both the double and triple thickness layers, but not in the single thickness layer. Clearly the assumption of an inviscid core between the vertical shear layers used in the analysis section is really not valid for the single thickness layer. In the thicker layers there is such a core where as noted from Eq. (3), there is no radial velocity and the other velocity components are very close to the inviscid values predicted by Eq. (12). The strength of the free surface shear layer clearly drops as the layer thickness increases and would disappear entirely if the container were full. To check the assertion that the free surface shear layer transports that amount of fluid that would otherwise be transported through the now-empty core, the following calculation was made. For the double and triple thickness layers the computed midheight axial velocity was numerically integrated from a point judged to be the center of the region of uniform upwelling inward to the free surface. The value of the resulting axial mass flow was compared to that obtained by multiplying the mean axial velocity in the uniform zone by the cross-sectional area from the same point into the centerline. The mass flows matched within 0.02% for the double thickness layer and 0.5% for the triple thickness layer, values which are well within the anticipated accuracy of the finite-difference approximations.

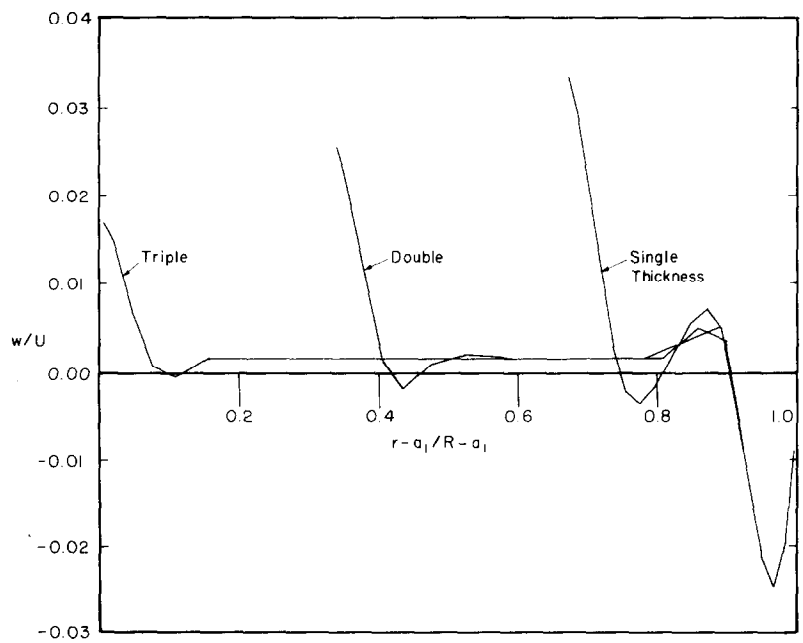

FIG. 9. Axial velocity at midheight for the flows of Figs. 3b, 7, and 8.

Since the motivation for using matching rather than resolution is even stronger with still lower Ekman numbers, a run was made using Shadday's parameters except for the fluid viscosity which was taken as that of pure water ($\nu = 10^{-6}$ m^2/sec, $E = 2.5 \times 10^{-7}$) rather than that of the glycerin/water solution he used. The cost to compute this flow with resolution of the Ekman layers would be exorbitant, since their estimated thickness is only about 0.05% of the rotor height. The vertical mesh was unchanged from the previous cases, but the horizontal grid was redistributed to give better resolution in the sidewall boundary layers. For this case the spinup time scale was estimated as 18.9 sec; the calculation was run until 39.8 sec had elapsed. Computer time was 515 sec. A sequence of plots (Figs. 10.1a–10.4b) shows the spinup process at four different times during the transient. So that the plots may be compared, a common streamfunction increment (0.199×10^{-6} m^2/sec) and a common azimuthal contour increment (0.0209 m/sec) have been used for all plots. Early in the transient (4.0 sec) the flow in the interior (Fig. 10.1a) is largely radial, and the sidewall boundary layers are developing. This radial inflow of higher angular velocity fluid is the mechanism by which the spinup takes place. At this time only a few azimuthal velocity contours have appeared (Fig. 10.1b). At about 8.0 sec the radial flow in the interior is less intense (Fig. 10.2a); more of the radial transport is through the bottom Ekman layer. Several more azimuthal contours have appeared (Fig. 10.2b). The process continues in Figs. 10.3a and b (15.9 sec). By the last plot (Fig. 10.4a and b, 39.8 sec), there is little radial transport in the interior and the spinup is essentially complete.

Conclusions

We have demonstrated here the appropriate form of the Ekman matching condition for the case of an incompressible fluid in a partially filled, strongly rotating right circular cylinder. With the fully implicit treatment of both the coriolis terms and the Ekman flow described here, the resulting MAC-derived, time-marching algorithm is extremely stable even at very low Ekman numbers. Assuming that the matching condition is finite-differenced so that there is pair-by-pair cancellation away from the edges, then the fact of enforcing mass conservation into and of each Ekman layer will create sources and sinks where appropriate. Since good agreement with experiment and fully resolved results was found, the advantage of using the matching condition rather than grid refinement and direct application of the no-slip condition is evident. With the latter the minimum (vertical) grid spacing must be of order 1/3 to 1/5 of the Ekman layer characteristic thickness; that is, 1/3 to 1/5 of $E^{1/2}L$. With the matching condition used at the ends, then it is the shear layers on the walls and free surface which must be adequately resolved. The minimum (horizontal) grid spacing must be of order 1/3 to 1/5 of the shear layer characteristic thickness; that is, 1/3 to 1/5 of $E^{1/3}L$. For small Ekman number the latter may be an order of magnitude or more greater. The computer time savings will be commensurate.

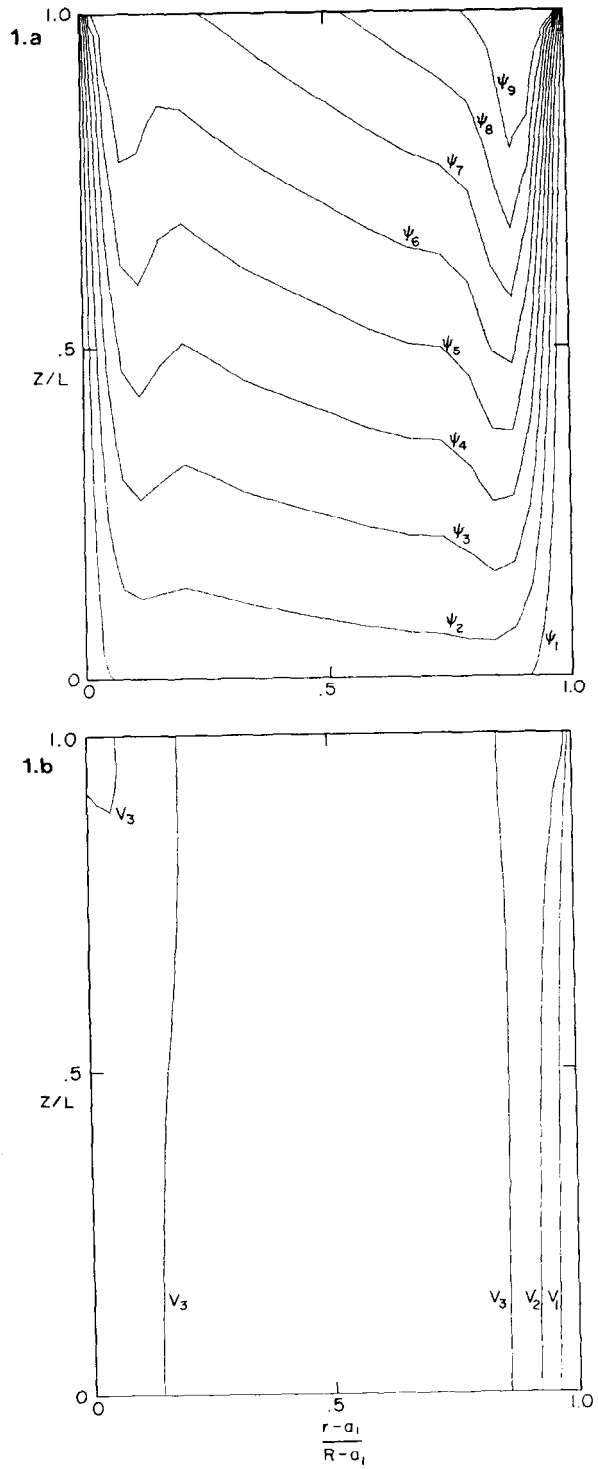

FIGS. 10.1a–10.4b. Streamlines and azimuthal velocity contours at selected times during the spinup transient. Same conditions as in Fig. 3b, but viscosity decreased by a factor of 10. $E = 2.5 \times 10^{-7}$. Streamline increment = 0.0209 m/sec. Fig. 10.1, 4.0 sec; Fig. 10.2, 8.0 sec; Fig. 10.3, 15.9 sec; Fig. 10.4, 39.8 sec.

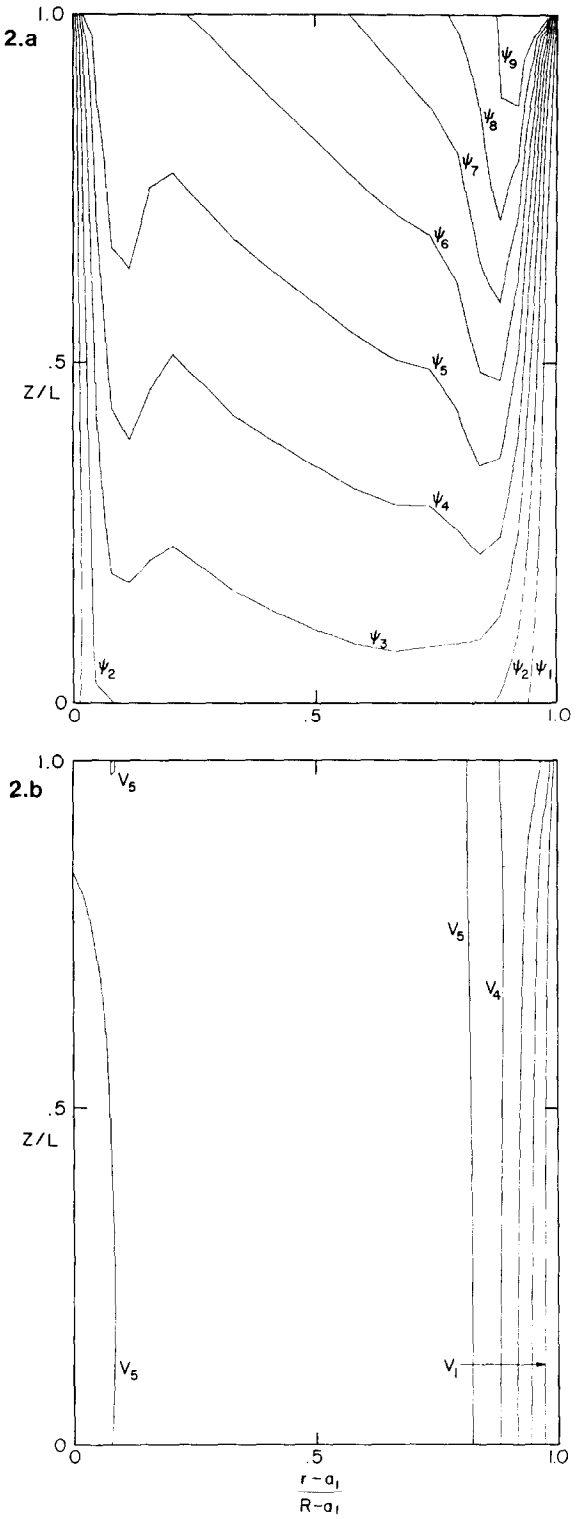
2.a
1.0
.5
Z/L
0
0
.5
1.0
ψ_9
ψ_8
ψ_7
ψ_6
ψ_5
ψ_4
ψ_3
ψ_2
ψ_2 ψ_1
2.b
1.0
.5
Z/L
0
0
.5
1.0
V_5
V_5
V_4
V_5
V_1
$\frac{r-a_1}{R-a_1}$

FIGURE 10.2

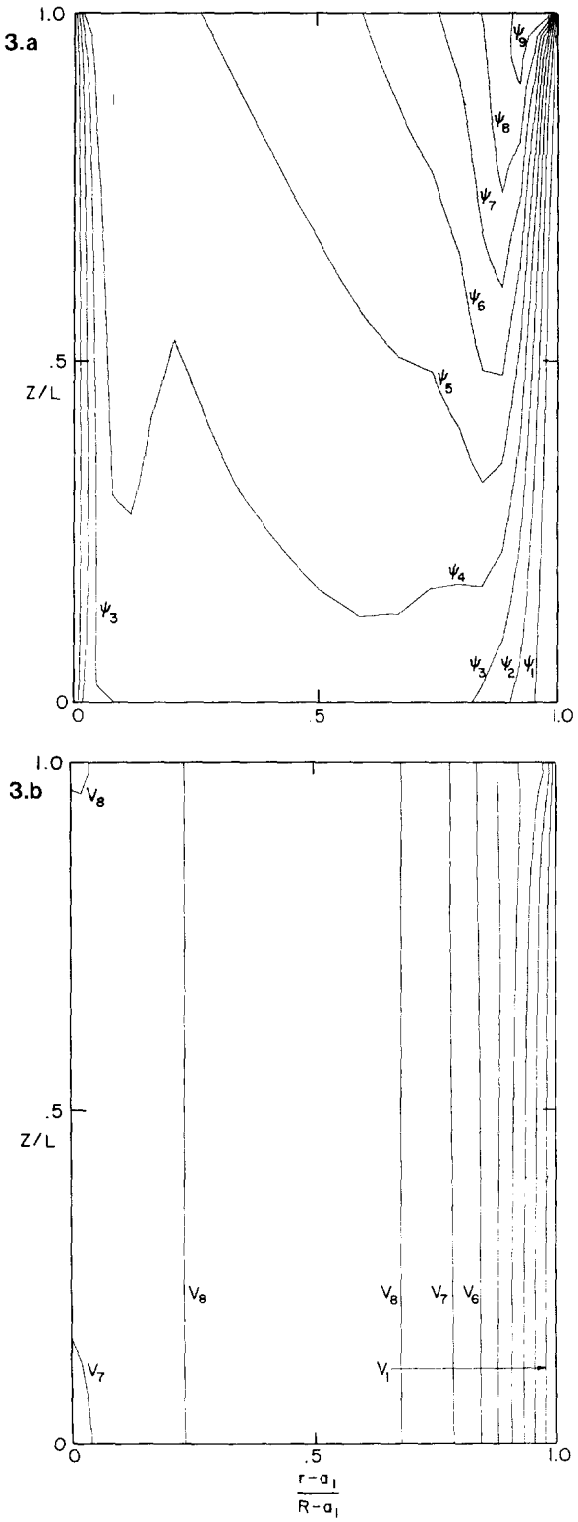
3.a
1.0
.5
Z/L
0
0
.5
1.0
ψ_9
ψ_8
ψ_7
ψ_6
ψ_5
ψ_4
ψ_3
ψ_3 ψ_2 ψ_1
3.b
1.0
.5
Z/L
0
0
.5
1.0
V_8
V_8
V_8 V_7 V_6
V_7
V_1
$\frac{r-a_1}{R-a_1}$

FIGURE 10.3

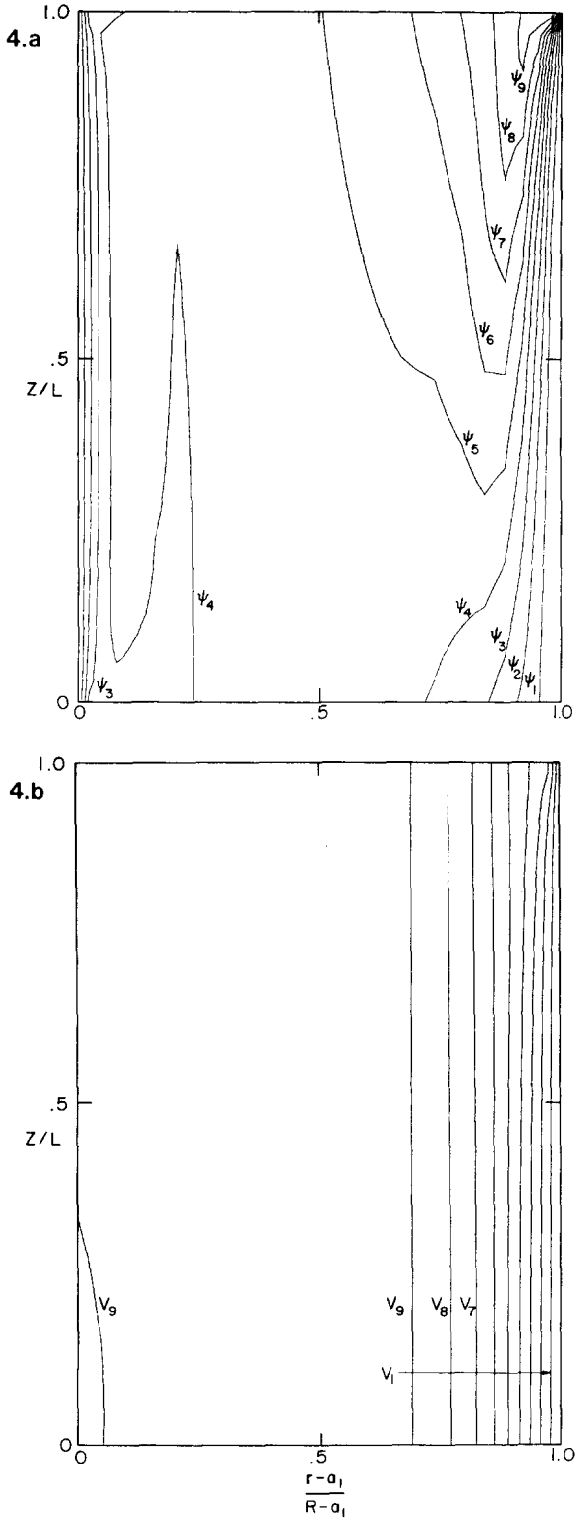
4.a
1.0
.5
Z/L
0
0
.5
1.0
ψ_9
ψ_8
ψ_7
ψ_6
ψ_5
ψ_4
ψ_4
ψ_3
ψ_3
ψ_2
ψ_1
4.b
1.0
.5
Z/L
0
0
.5
1.0
V_9
V_9
V_8
V_7
V_1
$\frac{r-a_1}{R-a_1}$

FIGURE 10.4

REFERENCES

1. M. A. SHADDAY, R. J. RIBANDO, AND J. J. KAUZLARICH, Flow of an incompressible fluid in a partially filled, rapidly rotating cylinder with a differentially rotating endcap, *J. Fluid Mech.* **130** (1983), 203–218.
2. H. P. GREENSPAN, "Simulation of Countercurrent Flow in a Gas Centrifuge," UVA-ER-746-82U, 1982.
3. H. P. GREENSPAN, "The Theory of Rotating Fluids," Cambridge Univ. Press, Cambridge, 1968.
4. R. J. RIBANDO, "Incompressible flow in a rapidly rotating cylinder with a source/sink distribution in the lateral wall and a free inner boundary, *Internat. J. Numer. Methods Fluids*, in press.
5. F. H. HARLOW AND J. E. WELCH, Numerical calculations of time-dimendent viscous incompressible flow of fluid with free surface, *Phys. Fluids* **8** (12) (1965), 2182–2189.
6. J. J. DONGARRA, C. B. MOLER, J. R. BUNCH, AND G. W. STEWART, "LINPACK User's Guide," *SIAM*, Philadelphia, 1979.
7. R. C. BEARDSLEY, K. D. SAUNDERS, A. C. WARN-VARNAS, AND J. M. HARDING, An experimental and numerical study of the secular spin-up of a thermally stratified rotating fluid, *J. Fluid Mech.* **93** (1) (1979), 161–184.
8. F. H. HARLOW AND A. A. AMSDEN, A numerical fluid dynamics method for all flow speeds, *J. Comp. Phys.* **8** (1971), 197–213).
9. C. W. HIRT AND B. D. NICHOLS, Adding limited compressibility to incompressible hydrocodes, *J. Comp. Phys.* **34** (1980), 390–400.